This is an open access article published under a Creative Commons Attribution (CC-BY) License, which permits unrestricted use, distribution and reproduction in any medium, provided the author and source are cited.

ACS AUTHORCHOICE

ACS OMEGA

Article

Cite This: ACS Omega 2020, 5, 422−429

http://pubs.acs.org/journal/acsodf

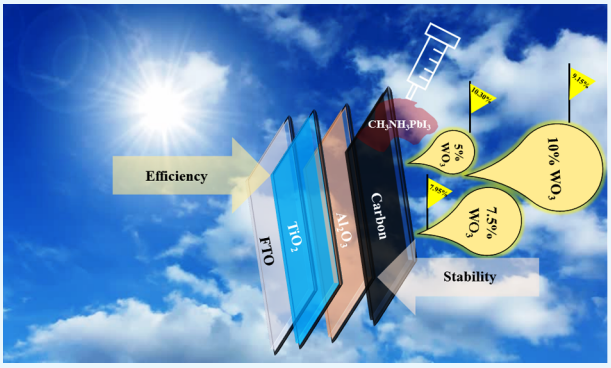
Performance of WO_3-Incorporated Carbon Electrodes for Ambient Mesoscopic Perovskite Solar Cells

Shubhranshu Bhandari, Anurag Roy,* Aritra Ghosh, Tapas Kumar Mallick, and Senthilarasu Sundaram*

Environment and Sustainability Institute (ESI), Penryn Campus, University of Exeter, Cornwall TR10 9FE, U.K.

Supporting Information

ABSTRACT: The stability of perovskite solar cells (PSC) is often compromised by the organic hole transport materials (HTMs). We report here the effect of WO_3 as an inorganic HTM for carbon electrodes for improved stability in PSCs, which are made under ambient conditions. Sequential fabrication of the PSC was performed under ambient conditions with mesoporous $TiO_2/Al_2O_3/CH_3NH_3PbI_3$ layers, and, on the top of these layers, the WO_3 nanoparticle-embedded carbon electrode was used. Different concentrations of WO_3 nanoparticles as HTM incorporated in carbon counter electrodes were tested, which varied the stability of the cell under ambient conditions. The addition of 7.5% WO_3 (by volume) led to a maximum power conversion efficiency of 10.5%, whereas the stability of the cells under ambient condition was ∼350 h, maintaining ∼80% of the initial efficiency under light illumination. At the same time, the higher WO_3 concentration exhibited an efficiency of 9.5%, which was stable up to ∼500 h with a loss of only ∼15% of the initial efficiency under normal atmospheric conditions and light illumination. This work demonstrates an effective way to improve the stability of carbon-based perovskite solar cells without affecting the efficiency for future applications.



INTRODUCTION

Technology development with improved levels of sustainability can create opportunity for today's state of the art photovoltaic devices as well as develop existing materials to improve performance. Organic−inorganic hybrid solar cells with perovskite-type pigments have been much studied in recent years. The solar cells incorporating a $CH_3NH_3PbI_3$ ($MAPbI_3$) compound with a perovskite structure have shown high photoconversion efficiencies (PCEs). Perovskite solar cells (PSCs) have recently become one of such technology and an area of interest owing to their lower preparation cost and high-conversion efficiency in the field of solar cell research.[1−3] The investigation in the field of PSCs has increased in recent years, and a highest recorded efficiency of 25.2% was achieved in early 2019, which has been independently confirmed by the international authority and authenticating institution, National Renewable Energy Laboratory (NREL).[4,5] Large-area PSCs with an active area >1 cm^2 exhibited a maximum photo-conversion efficiency (PCE) of 20.5% and a certified PCE of 19.6%.[6] Since the maximum theoretical PCE of the PSCs employing $MAPbI_3$ is around 31%, there is still great scope for development.[7] In addition to the high PCE achieved with the halide perovskites, these materials are composed of only earth-abundant elements and can be prepared by various low-cost methods. It is, therefore, highly anticipated that implantation of PSCs could be deployed on an industrial scale. The perovskite materials now focus on some challenging issues, for instance, the high PCE solar cells are still based on toxic Pb contamination and the halide salts tend to dissociate in the presence of moisture, which causes stability issue for long-term usage.[8] As per the toxicity concern of using Pb, extensive research effort has been committed to the development of lead-free perovskites such as $CH_3NH_3SnI_3$, $CH(NH_2)_2SnI_3$, $CsSnI_3$, Cs_2SnI_6, $BaZrS_3$, $CaZrSe_3$, $CaHfSe_3$, etc. for photo-voltaic applications.[9,10] It has been observed that the oxide perovskites exhibit more water resistivity compared to the halide perovskite. Besides, it is facile to tune the band gap of the oxide perovskite to match the solar spectrum and, therefore, act as a photoanode candidate for dye-sensitized solar cells (DSSCs). Extensive research on DSSCs enlarged the development pathway of planar structured PSCs in the initial stages.[11−13] The planar structure of PSCs became more prevalent when both the electron and hole transport properties have been simultaneously observed for the perovskite material.[14−16] Highly efficient PSCs sometimes rapidly lose their efficiency due to the hygroscopic character of the materials used.[17] Therefore, selection of materials and their fabrication process has limited the performance of PSCs. To overcome these issues, the mesoporous PSCs (m-PSCs) have come into account due to their simple fabrication process, high energy

Received: September 9, 2019
Accepted: November 19, 2019
Published: December 30, 2019

Downloaded via 91.125.131.75 on March 16, 2023 at 09:23:09 (UTC).
See https://pubs.acs.org/sharingguidelines for options on how to legitimately share published articles.

conversion, and enhanced resistivity toward environmental factors.[18,19] The mesoporous PSC includes carbon-based back contact, a suitable solution to substitute noble metals, due to its low cost, high conductivity, and eventually low-temperature processing and work function close to that of gold.[20] However, it would be advantageous to do so to increase the flexibility and the overall transparency of the device.

To develop high-efficiency and stable devices as well as environmentally benign perovskites is critical, yet challenging aspects remain in PSC research. Moisture sensitivity of the organic constituents of the PSC device resulting in long-term stability issue for its commercialization.[17,21] However, further involvements are required to enhance the commercial viability of PSC, which may be achieved through careful manipulation of the nanoscale structure and the implementation of novel processing techniques. To address the stability challenges, Al_2O_3 layer deposition, Li-doping, and Cs-doping inclusion to perovskite layer have been introduced for their long-term implementation.[22,23] Previously, Grätzel et al. reported that employment of solid-state organic hole transport materials (HTM) boosted the reported efficiency of solid-state m-PSCs to 9.7%.[11] Similarly, Nazeeruddin et al. introduced a sandwich-type layer of mesoporous TiO_2 and $MAPbI_3$ as a light harvester with polymeric HTMs, which resulted in an efficiency of 12%.[24] Seok's group used $CH_3NH_3PbI_{3-x}Br_x$-based mixed halide perovskites to further improve the efficiency to ∼12.3% and also to achieve better stability.[25] On the other hand, Lee et al. reported a PSC composed of mesoporous Al_2O_3 instead of TiO_2, demonstrating that Al_2O_3 merely acted as a scaffold layer without injection of photoexcited electrons resulting in faster electron diffusion through the perovskite layer.[26] Gracini et al. reported 1 year stable PSCs using a two-dimensional/three-dimensional (2D/3D) combined perovskite layer.[27] To get high efficiency and stability, effort to modify the mesoporous layer has been also made for a PSC device. Similarly, $CuInS_2$ quantum dot-modified TiO_2 nanoarrays were introduced by Gao et al. for better stability of devices.[28] Zhang et al. reported SnO_2-based devices with 17.83% efficiency.[29] However, to develop high-efficiency and stable devices as well as environmentally supported perovskites is still a crucial challenge and offers new and promising opportunities.[30−32]

Due to the ease of fabrication and higher efficiency, solar cells are often chosen as sources of electrical energy harvester, emerging markets such as self-powering systems and portable/wearable electronics.[33] Recently, Huan et al. reported an inexpensive photovoltaic-electrochemical cell system containing a low-cost perovskite photovoltaic minimodule, exhibiting ∼2.3% solar-to-hydrocarbon efficiency.[34] Intensive work is continuing for commercialization of perovskite photovoltaic technology as well.[35−37]

In these ways, several attempts have been made to enhance the performance of PSCs. In spite of encouraging performance, the drawbacks of organic HTM allow the development of inorganic HTM-based PSCs using Co_3O_4,[38] CuSCN,[39] NiO,[40,41] CuS,[42] and others.[43] Devices based on inorganic HTMs demonstrated better stability compared to a spiro-OMeTAD-based PSC in ambient condition.[44,45] Overall, to address the shortcomings associated with regular PSCs, carbon-based mesoscopic PSCs with inorganic HTM have attracted serious attention. Very recently, our group reported efficient PSC with WO_3 nanoparticle as HTM.[46] Established electrochromic property of WO_3 has been commercially inspected in electrochromic applications such as "smart windows".[47,48] It can lead to an integrated photoelectrochromic device, instead of sequential conjoining of a solar cell followed by a full electrochromic device. Using WO_3-based perovskite solar cells opens the possibility of further development in building-integrated photovoltaic (BIPV) application in terms of their low-energy, cost-effective, and novel architecture-based futuristic use.[49]

Here, we report the performance of $MAPbI_3$-based PSCs with a mesoporous TiO_2/Al_2O_3/carbon architecture where WO_3 nanoparticle-based carbon back contact was employed. The method is based on a fully wet deposition process, which takes less time and utilizes a screen-printing method. The influence of the different amounts of WO_3 is observed using 5, 7.5, and 10% WO_3 (by volume) in the carbon paste and compared with a device without WO_3 used as a reference, respectively. The purpose of this experiment was to develop stable PSC devices without using glovebox conditions and without any encapsulation. In our earlier reported paper, stability of the unsealed devices was very poor, ∼23% decay of initial PCE values within 100 h. The PSC fabrication technique was adopted from our earlier report with a modification of different WO_3 concentrations consisting of carbon layer deposition for back contact.[46] A schematic description of the PSC fabrication processes is given (steps a−g) in Figure 1.

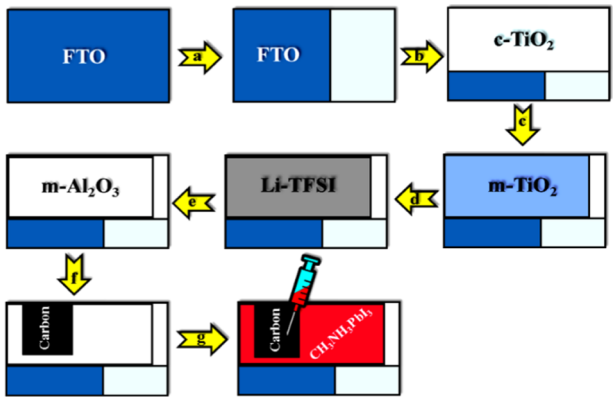


Figure 1. Stepwise fabrication process of the mesoporous perovskite solar cell. Step a: Etching of fluorine-doped tin oxide (FTO) glass; step b: compact TiO_2 layer deposition; step c: mesoporous TiO_2 layer formation; step d: lithium doping using lithium bis-(trifluoromethanesulfonyl) imide (Li-TFSI); step e: spin coating of mesoporous Al_2O_3 layer; step f: screen printing of the carbon electrode; step g: perovskite layer formation.

RESULTS AND DISCUSSION

The stepwise fabrication process with schematic structures is shown in Figure 1. Step a resembles etching of a FTO glass substrate. Step b and step c reflect the deposition of a compact TiO_2 layer and mesoporous TiO_2 layers, respectively. Lithium doping and mesoporous Al_2O_3 layer addition are shown in step d and step e, respectively. Screen printing of the WO_3 nanoparticles incorporated the carbon layer is represented by step f. Finally, the drop casting and spin coating of the perovskite were carried out, as shown in step g. The homogenous mixture for different carbon pastes was prepared by using the ball-milling technique. The cross-sectional FESEM image (Figure 2a) of the device shows the appropriate orientation of the layers in the following sequence FTO/c-TiO_2/ m-TiO_2/m-Al_2O_3/carbon from bottom to top. The

DOI: 10.1021/acsomega.9b02934
ACS Omega 2020, 5, 422−429

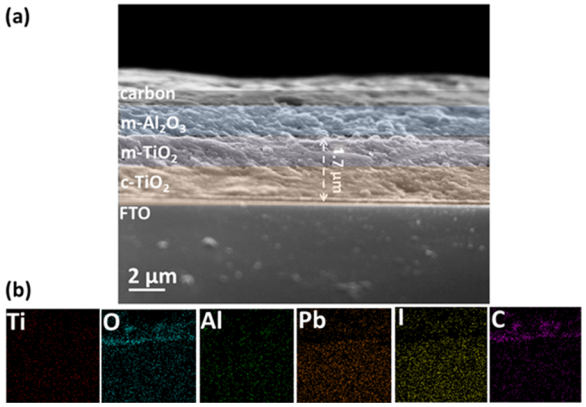


Figure 2. (a) Cross-sectional field emission scanning electron microscope (FESEM) image of the TiO_2/Al_2O_3/carbon device with $MAPbI_3$ and (b) energy dispersive X-ray (EDX) elemental color mapping of Ti, O, Al, Pb, I, and C of the device.

average thicknesses of mesoporous TiO_2 and mesoporous Al_2O_3 layers are ∼700 and ∼500 nm, respectively.

Corresponding energy dispersive X-ray (EDX) mapping confirms the distribution of elements and successful deposition of different layers, as shown in Figure 2b. The distribution of lead and iodine also confirms that the perovskite ($MAPbI_3$) layer had spread through the carbon layer as well as the mesoporous layers. To confirm the existence of WO_3, the EDX characterization was carried out and the EDX spectrum is given in Figure S1, supplementary information (ESI).

The XRD pattern of synthesized $CH_3NH_3PbI_3$ thin films on the FTO glass substrate is shown in Figure 3. Except for the

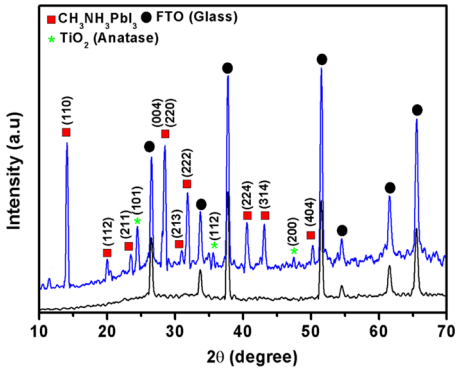


Figure 3. X-ray diffraction patterns of the $MAPbI_3/Al_2O_3/TiO_2$/FTO device (in blue) with major peaks for (110), (211), (220), and (213) planes are given in comparison to the blank FTO (in black).

signals of FTO glass and anatase TiO_2 shown with black and green dots, respectively, all remaining signals are responsible for the $MAPbI_3$ perovskite. The typical peaks at 14.10, 23.47, 28.42, and 30.89° correspond to the (110), (211), (220), and (213) planes of the tetragonal phase of $MAPbI_3$. XRD study confirms the phase purity and crystalline features of $MAPbI_3$, as reported previously.[50,51]

To evaluate the performance of the prepared m-PSCs made in ambient condition, the current vs voltage ($J-V$) characteristic measurement was performed under simulated AM 1.5 (100 mW/cm^2). Figure 4a and Table 1 exhibit the photovoltaic parameters such as efficiency, short-circuit current density (J_{SC}), open-circuit voltage (V_{OC}), and fill factor (FF) of the cells with an active area of 0.16 cm^2. Photovoltaic performance of the devices was examined, and the maximum photoconversion efficiency (PCE) was found ∼10.5% having J_{SC}, V_{OC}, and FF of 21.2 mA/cm^2, 854.4 mV, and 0.58, respectively, for the device with 7.5% WO_3, whereas the highest achieved efficiencies for 5 and 10% WO_3 devices were ∼8.3 and ∼9.4%, respectively. The high J_{SC} values may have occurred due to the Al_2O_3 layer deposition, which acts as a spacer layer that retards the recombination between TiO_2 and the carbon electrode.

IPCE resembles the external quantum efficiency of the DSSC device, which includes the effects of optical losses caused by transmission and reflection. The IPCE curve for m-PSCs exhibited a broad peak over the range of 300−800 nm with a maximum value of ∼89% for the 7.5% WO_3-based device at a wavelength of 550 nm indicating high charge collection efficiency in cells, as shown in Figure 4b. Due to a narrow band gap of ∼1.55 eV, the $MAPbI_3$ provides high extinction coefficient resulting in broad IPCE spectra from the visible range to a part of the near-infrared. Further, calculation of the integrated photocurrent density was evaluated from the overlap integral of the IPCE spectra as recorded in Figure 4b with the AM 1.5 solar emission for different devices and values mentioned in Table S1 (ESI). The average integrated photocurrent densities of PSCs with different amounts of WO_3 additive closely match with photocurrent densities obtained from the $J-V$ curve.

The nature of forward and reverse scanned $J-V$ plots gives impression of hysteresis. Significant hysteresis is observed for all of the different sets of devices, as shown in Figure 5a−c. Hysteresis is more pronounced for the devices with 7.5% WO_3, as can be seen from Figure 5b. Figure 5d provides the power output of all of the PSC devices per unit cross-sectional area. The enhanced power density was observed for WO_3-added devices compared to the device without WO_3 treatment. Similar to the $J-V$ plot, the power density reaches its maximum values of 5.89 mW/cm^2 for 7.5% WO_3.

Figure S2 (ESI) provides the variance of V_{OC}, J_{SC}, fill factor, and PCE values for a batch of 10 devices from each set. The overall PCE values range from 10.1 to 10.5% in the case of the 7.5% of the WO_3-added devices. Interestingly, the fill factor of devices with a lower amount of WO_3 is higher than that of the others.

Further, the electrochemical impedance spectroscopy (EIS) measurements were carried out to understand the transport properties at different interfaces in the m-PSC assembly. The EIS spectra (Nyquist plot) with equivalent circuit diagram and corresponding Bode phase diagram of the concerned PSCs were recorded under dark at 0.7 V bias from 10 to 1 MHz, as shown in Figure 6a,b, respectively. In the circuit diagram (inset of Figure 6a), R_S represents the series resistance, which include resistance of FTO and carbon counter electrode. R_{rec} is the charge-transfer resistance at the perovskite/carbon interface and R_{CT} is the charge-transfer resistance at the $TiO_2/MAPbI_3$ interface. It can be interpreted from Figure 6a that the large parabola in the high-frequency region indicates higher transportation and exchange resistance from the perovskite to the carbon counter electrode, so it will affect the fill factor as reflected from $J-V$ characterization. On the other hand, the smaller parabola reflects the recombination resistance between TiO_2 and the perovskite interface. The large R_{CT} value implies a slow charge recombination process or low charge recombination rate. This low recombination rate is responsible for high values of J_{SC} and V_{OC}, which is reflected in the $J-V$

DOI: 10.1021/acsomega.9b02934
ACS Omega 2020, 5, 422−429

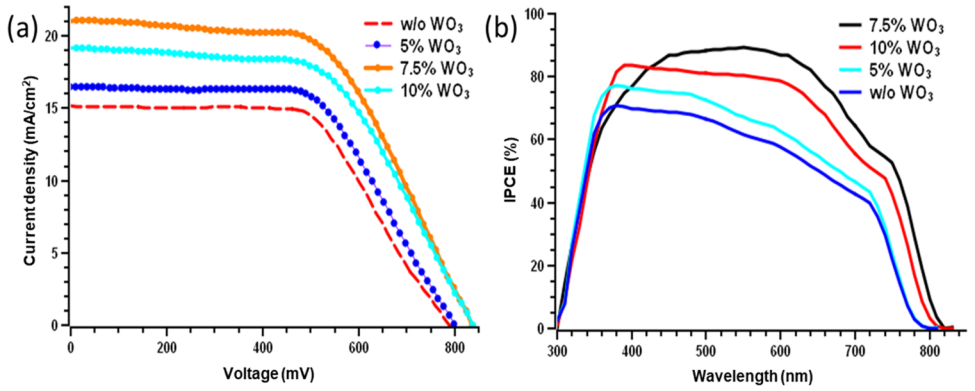


Figure 4. (a) Current−voltage (J−V) curves and (b) incident photon to current efficiency (IPCE) spectra for different m-PSCs containing 5, 7.5, 10% of WO_3 compared with and without (w/o) WO_3-based devices, respectively.

Table 1. Photovoltaic Parameters of Ambient Mesoporous Perovskite Solar Cells under 1 SUN AM1.5 G, with an Active Area of 0.16 cm^2

sample	V_{OC} (mV)	J_{SC} (mA/cm^2)	fill factor (FF)	PCE (%)	power output (mW/cm^2)
without WO_3	788.8 ± 15	15.16 ± 0.1	0.62 ± 0.01	7.40 ± 0.3	4.54
5% WO_3	801.3 ± 20	16.4 ± 0.15	0.605 ± 0.01	7.95 ± 0.4	4.86
7.5% WO_3	842.3 ± 20	21.1 ± 0.2	0.58 ± 0.01	10.30 ± 0.2	5.89
10% WO_3	840.4 ± 15	19.3 ± 0.15	0.56 ± 0.01	9.15 ± 0.3	5.22

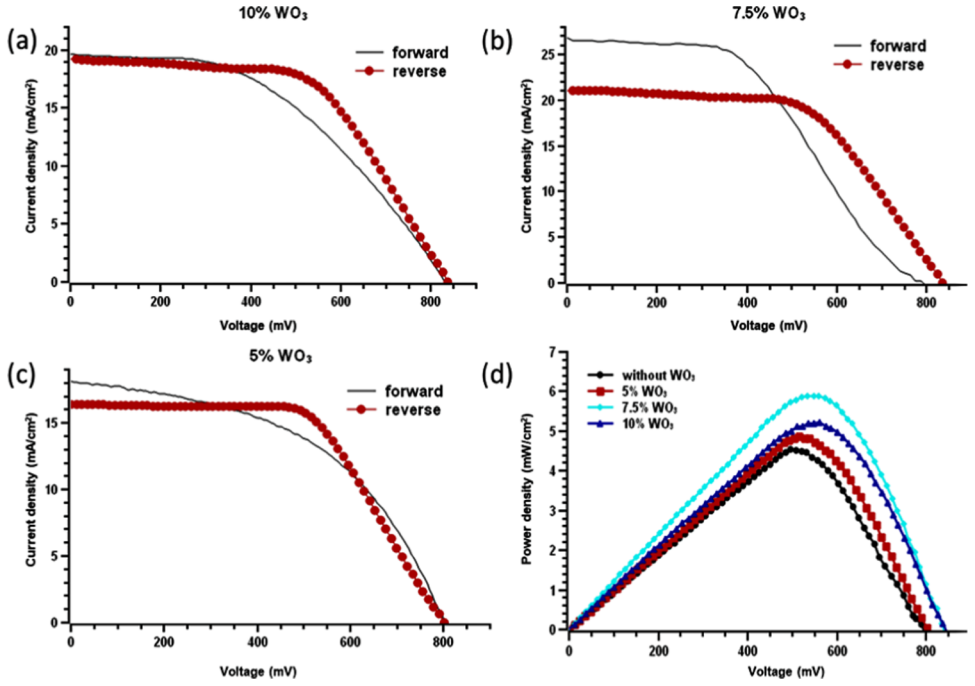


Figure 5. J−V characteristic plot showing the forward and reverse scans with an active area of 0.16 cm^2 under 1 sun (100 mW/cm^2) light illumination for devices with (a) 10%, (b) 7.5%, and (c) 5% WO_3 and (d) corresponding power density vs voltage plot.

curve. Devices with higher R_S value should have lower efficiency, which can be observed from Table S2 (ESI). Long-term stability is the most critical challenge for PSCs under ambient conditions without any encapsulation. The stability of the PSC is environment dependent, mostly affected by the humidity, light conditions, and climatic conditions.[52]

The PSCs were kept at ambient conditions, to understand the degradation pattern of the solar cell. The prepared PSCs were characterized under illumination for ∼500 h, as shown in Figure 7a−c. It was observed that the amount of WO_3 controls the stability of the devices. Figure 7a,b indicates a steady decrease in J_{SC} and V_{OC} with time, respectively. The devices with a higher amount of WO_3 maintain their efficiency for a longer time. The device containing 7.5% of WO_3 maintained its stability with a loss of 20% efficiency up to ∼350 h. Significantly, stability of ∼500 h is observed for the device with 10% of WO_3 and it maintains the PCE of ∼85% of the initial value (Figure 7c). The presence of inorganic HTM may stabilize the device in these purposes. This result indicates that higher concentration of WO_3 affects the power conversion efficiency, but at the same time it increases the stability of the devices. The use of WO_3/carbon electrode reduces the

DOI: 10.1021/acsomega.9b02934
ACS Omega 2020, 5, 422−429

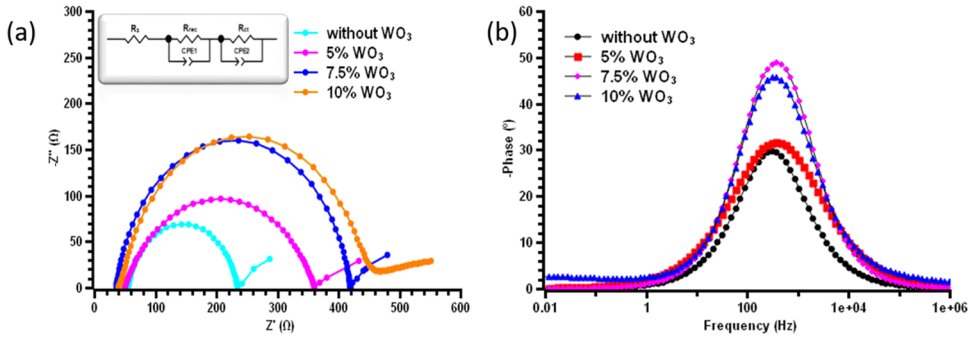


Figure 6. (a) EIS characteristics (Nyquist plots) with the fitted circuit diagram and (b) corresponding Bode phase plot of different PSCs.

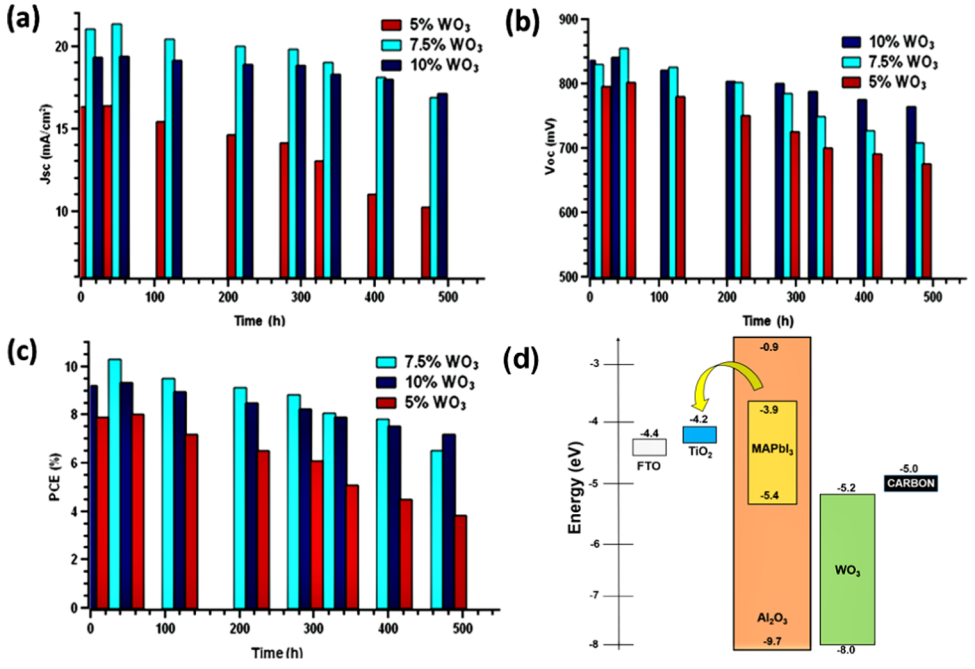


Figure 7. Photovoltaic characterization of 5, 7.5, and 10% WO_3-contained devices in terms of their (a) current density (J_{SC}), (b) open circuit voltage (V_{OC}), (c) PCE monitored up to 500 h, respectively and (d) schematic diagram of energy band position of the WO_3-added perovskite solar cell.

porosity of the layer due to the presence of small sized WO_3 nanoparticles. The small porosity of the electrode layer could help to prevent the permeability of moisture/oxygen through the counter electrode. This may be the reason behind the greater stability of devices with a higher amount of WO_3 nanoparticle in the electrode material. A simple schematic energy band diagram of the carbon-based mesoscopic PSCs with WO_3 nanoparticles additive is shown in Figure 7d. According to the energy-level positions of different components, the excited electron is transferred from the conduction band of the $MAPbI_3$, perovskite layer (−3.9 eV) to that of the TiO_2 layer (−4.0 eV) followed by the hole extraction from the perovskite layer (−5.4 eV) to the carbon layer (−5.0 eV) via WO_3 (−5.3 eV). Al_2O_3 layer served as a spacer and retards the electron−hole recombination in the PSCs. The additive WO_3 inside the carbon film can work as HTM to promote the hole-extraction in the perovskite/carbon interface due to its appropriate position of the conduction band.[46,53,54] This is further facilitated by energy-level matching, which helps a notable improvement in the hole extraction, recombination resistance compared to without WO_3-based device.

It is proposed that incorporating WO_3 in Pt CE favorably occupies the gap states near the Fermi level and maintains high work function, which accelerates the charge transportation and enhances charge extraction of Pt in PSC. Treatment with WO_3 may also take part similarly in modifying the electronic structure of carbon and can be explored as a hole-transporting layer for PSC. The electron hopping conduction mechanism is the most probable reason behind the high electrical conductivity of the annealed WO_3 at 500 °C.[55] The presence of oxygen vacancies in substoichiometric WO_3 creates various defect states of WO_3, such as W^{4+} or W^{5+} and W^{6+}, located within the band gap, respectively. These may promote charge transfer and enhance the electrical conductivity in the mixed valence states of W^{4+}, W^{5+}, and W^{6+} accordingly.[56,57] Also, the conductivity measurement data mentioned in Table S3 (ESI) clarify the performance of different devices. Besides, optimum amount of WO_3 in the hybrid carbon paste plays a vital role in modifying the carbon counter electrode. Less amount of WO_3 incorporation may result in insufficient work function of WO_3 well, whereas an excessive amount may decrease the conductivity of the carbon and also effect transparency of the device. Further, this experimentation is comparable to

DOI: 10.1021/acsomega.9b02934
ACS Omega 2020, 5, 422−429

Table 2. Stability Comparisons of Carbon-Based Mesoscopic Perovskite Solar Cells from Previous Reports Based on $MAPbI_3$

device structure	average PCE (%)	stability of unsealed device	active area (cm^2)	refs
FTO/c-TiO_2/m-TiO_2/m-ZrO_2/Co_3O_4/carbon/$MAPbI_3$	11.7	∼2500 h in ambient condition in the presence of light	0.8	38
FTO/m-TiO_2/m-ZrO_2/NiO/carbon/$MAPbI_3$	13.7	PCE decreased to 80% of initial after ∼150 h in the presence of light		40
FTO/c-TiO_2/m-TiO_2/ $CH_3NH_3PbI_3$/C-CuS	10.22	over 600 h in ambient condition with 30−50% humidity in dark		42
FTO/c-TiO_2/m-TiO_2/m-ZrO_2/carbon/$MAPbI_3$	6.5	∼850 h in dry air condition at room temperature in dark	0.125	58
FTO/c-TiO_2/m-TiO_2/m-Al_2O_3/carbon/$MAPbI_3$	12.3	PCE decreased to 1% of initial after ∼480 h under light at room temperature	0.09	59
FTO/c-TiO_2/m-TiO_2/m-Al_2O_3/SWCNT-NiO/$MAPbI_3$	12.7	∼300 h in ambient condition		60
FTO/c-TiO_2/m-TiO_2/m-Al_2O_3/carbon-WO_3/$MAPbI_3$	10.3	85% of initial PCE retains after ∼500 h in ambient condition in the presence of light	0.16	this work

those of other previous works related to inorganic HTM for carbon-based perovskite solar cells in the context of stability, as given in Table 2. Most of these devices have much less stability under light illumination except for the device with Co_3O_4. In our case, under light illumination devices with 10% WO_3 are fairly stable (∼500 h) without any substantial loss of efficiency.

CONCLUSIONS

In conclusion, we have demonstrated here the fully printable mesoporous perovskite solar cells with nanoparticles incorporated in the carbon back contact top electrode fabricated under ambient condition. These devices show interesting stability depending on the amount of WO_3 (5, 7.5, and 10% by volume) in the carbon electrode. The efficiency increase was observed for the devices with nanoparticles in comparison to those without. The highest efficiency was obtained with the 7.5% WO_3 device, but the stability of devices with 10% WO_3 is more pronounced. The results suggest that depending on the amount of efficient additives, the device performance can be influenced remarkably. The obtained maximum efficiency was lower than the values reported for other PSCs; however, with all factors taken into account, the proposed option might emerge as be much more realistic and, thus, more promising. Further, this work demonstrates that the concentration variation of WO_3 can improve the stability significantly for uncapped devices in open air conditions under light. This constitutes an important step toward the efficiency improvement of the devices for futuristic photoelectrochromic or self-powered switchable glazing for low-energy adaptive façade integration.

EXPERIMENTAL SECTION

Device Fabrication. In details, the first step (step a) resembles etching of the fluorine-doped tin oxide (FTO) glass substrate. Next, TiO_2 compact layer was spin-coated at 2000 rpm for 30 s on the etched clean FTO transparent glass by using 0.15 M titanium di-isopropoxide bis-(acetylacetonate) $Ti(acac)_2O^iPr_2$ (75 wt % in isopropanol, Sigma-Aldrich) (99.9%, Sigma-Aldrich) solution in 2-propanol, followed by drying at 115 °C for 5 min. This step is repeated for one more time, and finally the coated samples were then placed on a hot plate at a temperature of 415 ± 10 °C for 30 min followed by cooling to room temperature (step b). The mesoporous TiO_2 layer was deposited by spin coating at 2500 rpm for 30 s using diluted TiO_2 paste (18NRT from Great Cell Solar Company; w/w = 1:3.5 in ethanol) and heated at 500 °C for 60 min (step c). After cooling down to room temperature, lithium doping was carried out via spin coating (3000 rpm, 15 s) of 0.1 M lithium bis-(trifluoromethanesulfonyl) imide (Li-TFSI) solution in acetonitrile followed by annealing at 415 ± 15 °C for 30 min (step d). Then, the Al_2O_3 mesoporous layer was spin-coated with diluted Al_2O_3 paste (Sigma-Aldrich; v/v = 1:2 in isopropanol) at 2000 rpm for 30 s and heated at 150 °C for 30 min (step e). To prepare the carbon paste for back contact, 1.2 g of graphite powder (Sigma-Aldrich) was mixed with 0.2 g of carbon black powder (Alfa Aesar) in 4.0 mL of α-terpineol (Sigma-Aldrich). Then, 0.1 g of ZrO_2 powder (Sigma-Aldrich), 1.5 g of ethyl cellulose (15 wt % in ethanol) (Sigma-Aldrich), and three different amounts (5, 7.5, and 10% by volume) of WO_{3-x} nanoparticle ink (2.5 wt % in isopropanol, Sigma-Aldrich) were added to the above paste, followed by ball milling overnight. Thus, the prepared carbon paste was screen-printed above the mesoporous Al_2O_3 layer to obtain a mesoscopic carbon layer, which was sintered at 450 °C for 30 min (Step f). The $MAPbI_3$ perovskite solution was prepared via the ion-exchange method. In short, 0.198 g of CH_3NH_3I (Sigma-Aldrich) and 0.573 g of PbI_2 (Sigma-Aldrich) were dissolved in 1 mL of γ-butyrolactone (Sigma-Aldrich) and then stirred at 60 °C overnight.[41] After cooling down to room temperature, the perovskite precursor solution with an appropriate amount was infiltrated by drop casting via the top of the carbon counter electrode and further spin coating at 1000 rpm for 15 s. At last, drying was done at 50 °C for 1 h (Step g). Finally, the PSC was employed for further characterization and measurements. Note: All of the data represented here are the average measurement of five individual fabricated m-PSC devices for each case. Their corresponding photovoltaic performance was monitored since last 6 months with negligible hysteresis effect and high reliability and repeatability at ambient condition. Every individual m-PCSs were measured in every 24 h up to 500 h to check their photovoltaic performance and stability. The cells were fabricated and stored at ambient condition for all of the cases. Box and whisker plot of efficiency measurements indicated the error range recorded during the period of device measurement (Figure S2, ESI).

Characterization. X-ray diffraction (XRD) analyses of the fabricated PSC films were carried out on a X'pert pro MPD XRD of PANalytical with Cu Kα radiation (λ = 1.5406 Å). The cross-sectional thickness measurement and elemental mapping of the PSC were recorded on a scanning electron microscope (SEM), (LEO 430i, Carl Zeiss). Further, testing of the PSC was executed under 1000 W/m^2 of light from a Wacom AAA continuous solar simulator (model: WXS-210S-20, AM 1.5 G). The $I-V$ characteristic of the devices was recorded using an EKO MP-160 $I-V$ Tracer. EIS measurements were carried out

DOI: 10.1021/acsomega.9b02934
ACS Omega 2020, 5, 422−429

with an AUTOLAB frequency analyzer setup equipped with an AUTOLAB PGSTAT 10 and a Frequency Response Analyzer (FRA) Module. The measurements were performed under the same solar simulator condition with the frequency range from 0.1 to 100 kHz. All of the devices were measured at the 0.70 V open-circuit voltage of the devices. The experimental data were fitted with the Z-view software (version 3.4d, Scribner Associates, Inc.) using appropriate equivalent circuits. Incident photon to current efficiency (IPCE) was carried out on a BENTHAM PVE300 Photovoltaic EQE (IPCE) and IQE solution under 350−750 nm wavelength using a tungsten halogen lamp source.[46] The conductivity measurements were performed using the Ossila (UK) Four-Point Probe Instrument. All of the data presented are an average of measurements taken on three different devices.

■ ASSOCIATED CONTENT

Supporting Information

The Supporting Information is available free of charge at https://pubs.acs.org/doi/10.1021/acsomega.9b02934.

SEM cross-sectional images of PSCs; box and whisker plot of the photovoltaic performance of the PSC devices; table of integrated current density and EQE obtained from IPCE measurement; table of EIS spectra fitting data; table of resistance and conductivity measurements (PDF)

■ AUTHOR INFORMATION

Corresponding Authors

*E-mail: A.Roy30@exeter.ac.uk, ar.chem30@gmail.com. Tel: 01326-259486 (A.R.).

*E-mail: S.Sundaram@exeter.ac.uk. (S.S.).

ORCID

Anurag Roy: 0000-0002-2097-9442

Aritra Ghosh: 0000-0001-9409-7592

Notes

The authors declare no competing financial interest.

■ ACKNOWLEDGMENTS

S.B would like to acknowledge the College of Engineering, Mathematics, and Physical Sciences, University of Exeter for the PhD fellowship. This work has been conducted as part of the research project "Joint UK-India Clean Energy Centre (JUICE)", which is funded by the RCUK's Energy Programme (contract no: EP/P003605/1). The project's funders were not directly involved in writing of this article. In support of open access research, all underlying article materials (data, experimental details) can be accessed upon request via email to the corresponding author.

■ REFERENCES

(1) Park, N.-G. Organometal perovskite light absorbers toward a 20% efficiency low-cost solid-state mesoscopic solar cell. *J. Phys. Chem. Lett.* **2013**, *4*, 2423−2429.

(2) Xing, G.; Mathews, N.; Sun, S.; Lim, S. S.; Lam, Y. M.; Grätzel, M.; Mhaisalkar, S.; Sum, T. C. Long-range balanced electron- and hole-transport lengths in organic-inorganic $CH_3NH_3PbI_3$. *Science* **2013**, *342*, 344−347.

(3) Grätzel, M. The light and shade of perovskite solar cells. *Nat. Mater.* **2014**, *13*, 838.

(4) Green, M. A.; Hishikawa, Y.; Dunlop, E. D.; Levi, D. H.; Hohl-Ebinger, J.; Ho-Baillie, A. W. Y. Solar cell efficiency tables (version 52). *Prog. Photovoltaics* **2018**, *26*, 427−436.

(5) *Best Research-Cell Efficiency Chart*; National Renewable Energy Laboratory: USA. https://www.nrel.gov/pv/cell-efficiency.html.

(6) Li, X.; Bi, D.; Yi, C.; De'coppet, J.-D.; Luo, J.; Zakeeruddin, S. M.; Hagfeldt, A.; Grätzel, M. A Vacuum flash-assisted solution process for high-efficiency large-area perovskite solar cells. *Science* **2016**, *353*, 58−62.

(7) Sha, W. E. I.; Ren, X.; Chen, L.; Choy, W. C. H. The efficiency limit of $CH_3NH_3PbI_3$ perovskite solar cells. *Appl. Phys. Lett.* **2015**, *106*, No. 221104.

(8) Fu, H. Review of lead-free halide perovskites as light-absorbers for photovoltaic applications: from materials to solar cells. *Sol. Energy Mater. Sol. Cells* **2019**, *193*, 107−132.

(9) Konstantakou, M.; Stergiopoulos, T. A critical review on tin halide perovskite solar cells. *J. Mater. Chem. A* **2017**, *5*, 11518−11549.

(10) Sun, Y.-Y.; Agiorgousis, M.-L.; Zhang, P.; Zhang, S. Chalcogenide perovskites for photovoltaics. *Nano Lett.* **2015**, *15*, 581−585.

(11) Kim, H.-S.; Lee, C.-R.; Im, J.-H.; Lee, K.-B.; Moehl, T.; Marchioro, A.; Moon, S.-J.; Humphry-Baker, R.; Yum, J.-H.; Moser, J. E.; Grätzel, M.; Park, N.-G. Lead iodide perovskite sensitized all-solid-state submicron thin film mesoscopic solar cell with efficiency exceeding 9%. *Sci. Rep.* **2012**, *2*, No. 591.

(12) Burschka, J.; Pellet, N.; Moon, S.-J.; Humphry-Baker, R.; Gao, P.; Nazeeruddin, M. K.; Grätzel, M. Sequential deposition as a route to high-performance perovskite-sensitized solar cells. *Nature* **2013**, *499*, 316.

(13) Upadhyaya, H. M.; Senthilarasu, S.; Hsu, M.-H.; Kumar, D. K. Recent progress and the status of dye-sensitised solar cell (dssc) technology with state-of-the-art conversion efficiencies. *Sol. Energy Mater. Sol. Cells* **2013**, *119*, 291−295.

(14) Christians, J. A.; Fung, R. C. M.; Kamat, P. V. An inorganic hole conductor for organo-lead halide perovskite solar cells. improved hole conductivity with copper iodide. *J. Am. Chem. Soc.* **2014**, *136*, 758−764.

(15) Zhou, H.; Chen, Q.; Li, G.; Luo, S.; Song, T.-b.; Duan, H.-S.; Hong, Z.; You, J.; Liu, Y.; Yang, Y. Interface engineering of highly efficient perovskite solar cells. *Science* **2014**, *345*, 542−546.

(16) McMeekin, D. P.; Sadoughi, G.; Rehman, W.; Eperon, G. E.; Saliba, M.; Hörantner, M. T.; Haghighirad, A.; Sakai, N.; Korte, L.; Rech, B.; Johnston, M. B.; Herz, L. M.; Snaith, H. J. A mixed-cation lead mixed-halide perovskite absorber for tandem solar cells. *Science* **2016**, *351*, 151−155.

(17) Wang, R.; Mujahid, M.; Duan, Y.; Wang, Z.-K.; Xue, J.; Yang, Y. A review of perovskites solar cell stability. *Adv. Funct. Mater.* **2019**, *29*, No. 1808843.

(18) Duan, M.; Hu, Y.; Mei, A.; Rong, Y.; Han, H. Printable carbon-based hole-conductor-free mesoscopic perovskite solar cells: from lab to market. *Mater. Today Energy* **2018**, *7*, 221−231.

(19) Abate, A.; Correa-Baena, J.-P.; Saliba, M.; Su'ait, M. S.; Bella, F. Perovskite solar cells: from the laboratory to the assembly line. *Chem. - Eur. J.* **2018**, *24*, 3083−3100.

(20) Chen, H.; Yang, S. Carbon-based perovskite solar cells without hole transport materials: the front runner to the market? *Adv. Mater.* **2017**, *29*, No. 1603994.

(21) Kojima, A.; Teshima, K.; Shirai, Y.; Miyasaka, T. Organometal halide perovskites as visible-light sensitizers for photovoltaic cells. *J. Am. Chem. Soc.* **2009**, *131*, 6050−6051.

(22) Maniarasu, S.; Manjunath, V.; Ramasamy, E.; Veerappan, G. Chapter 9 - Hole conductor-free perovskite solar cells. In *Perovskite Photovoltaics*; 2nd ed.; Thomas, S.; Thankappan, A., Eds.; Academic Press, 2018; pp. 289−321.

(23) Bella, F.; Renzi, P.; Cavallo, C.; Gerbaldi, C. Caesium for perovskite solar cells: an overview. *Chem. - Eur. J.* **2018**, *24*, 12183−12205.

(24) Heo, J. H.; Im, S. H.; Noh, J. H.; Mandal, T. N.; Lim, C.-S.; Chang, J. A.; Lee, Y. H.; Kim, H.-J.; Sarkar, A.; Nazeeruddin, M. K.;

DOI: 10.1021/acsomega.9b02934
ACS Omega 2020, 5, 422−429

Grätzel, M.; Seok, S. I. Efficient inorganic−organic hybrid heterojunction solar cells containing perovskite compound and polymeric hole conductors. *Nat. Photonics* **2013**, *7*, 486.
(25) Noh, J. H.; Im, S. H.; Heo, J. H.; Mandal, T. N.; Seok, S. I. Chemical management for colorful, efficient, and stable inorganic-organic hybrid nanostructured solar cells. *Nano Lett.* **2013**, *13*, 1764−1769.
(26) Lee, M. M.; Teuscher, J.; Miyasaka, T.; Murakami, T. N.; Snaith, H. J. Efficient hybrid solar cells based on meso-superstructured organometal halide perovskites. *Science* **2012**, *338*, 643−647.
(27) Grancini, G.; Roldán-Carmona, C.; Zimmermann, I.; Mosconi, E.; Lee, X.; Martineau, D.; Narbey, S.; Oswald, F.; De Angelis, F.; Graetzel, M.; Nazeeruddin, M. K. One-year stable perovskite solar cells by 2D/3D interface engineering. *Nat. Commun.* **2017**, *8*, No. 15684.
(28) Gao, F.; Zheng, Q.; Zhang, Y. Stability improvement of perovskite solar cells for application of $CuInS_2$ quantum dot-modified TiO_2 nanoarrays. *ACS Omega* **2019**, *4*, 3432−3438.
(29) Zhang, W.; Li, Y.; Liu, X.; Tang, D.; Li, X.; Yuan, X. Ethyl acetate green antisolvent process for high-performance planar low-temperature SnO_2-based perovskite solar cells made in ambient air. *Chem. Eng. J.* **2020**, *379*, No. 122298.
(30) Dai, W. B.; Xu, S.; Zhou, J.; Hu, J.; Huang, K.; Xu, M. Lead-free, stable, and effective double $FA_4Ge_{II}Sb_{III}Cl_{12}$ perovskite for photovoltaic applications. *Sol. Energy Mater. Sol. Cells* **2019**, *192*, 140−146.
(31) Devi, C.; Mehra, R. Device simulation of lead-free $MASnI_3$ solar cell with $CuSbS_2$ (copper antimony sulfide). *J. Mater. Sci.* **2019**, *54*, 5615−5624.
(32) Fu, H. Review of lead-free halide perovskites as light-absorbers for photovoltaic applications: from materials to solar cells. *Sol. Energy Mater. Sol. Cells* **2019**, *193*, 107−132.
(33) Yun, S.; Qin, Y.; Uhl, A. R.; Vlachopoulos, N.; Yin, M.; Li, D.; Han, X.; Hagfeldt, A. New-generation integrated devices based on dye-sensitized and perovskite solar cells. *Energy Environ. Sci.* **2018**, *11*, 476−526.
(34) Huan, T. N.; Dalla Corte, D. A.; Lamaison, S.; Karapinar, D.; et al. Low-cost high-efficiency system for solar-driven conversion of co_2 to hydrocarbons. *Proc. Natl. Acad. Sci. U.S.A.* **2019**, *116*, 9735−9740.
(35) Wojciechowski, K.; Forgács, D.; Rivera, T. Industrial opportunities and challenges for perovskite photovoltaic technology. *Sol. RRL* **2019**, *3*, No. 1900144.
(36) Siegler, T. D.; Shimpi, T. M.; Sampath, W. S.; Korgel, B. A. Development of wide bandgap perovskites for next-generation low-cost CdTe tandem solar cells. *Chem. Eng. Sci.* **2019**, *199*, 388−397.
(37) Choi, I. Y.; Kim, C. U.; Park, W.; Lee, H.; Song, M. H.; Hong, K. K.; Seok, S. I.; Choi, K. J. Two-terminal mechanical perovskite/silicon tandem solar cells with transparent conductive adhesives. *Nano Energy* **2019**, *65*, No. 104044.
(38) Bashir, A.; Shukla, S.; Lew, J. H.; Shukla, S.; Bruno, A.; Gupta, D.; Baikie, T.; Patidar, R.; Akhter, Z.; Priyadarshi, A.; Mathews, N.; Mhaisalkar, S. G. Spinel Co_3O_4 nanomaterials for efficient and stable large area carbon-based printed perovskite solar cells. *Nanoscale* **2018**, *10*, 2341−2350.
(39) Arora, N.; Dar, M. I.; Hinderhofer, A.; Pellet, N.; Schreiber, F.; Zakeeruddin, S. M.; Grätzel, M. Perovskite solar cells with CuSCN hole extraction layers yield stabilized efficiencies greater than 20%. *Science* **2017**, *358*, 768−771.
(40) Xu, X.; Liu, Z.; Zuo, Z.; Zhang, M.; Zhao, Z.; Shen, Y.; Zhou, H.; Chen, Q.; Yang, Y.; Wang, M. Hole selective NiO contact for efficient perovskite solar cells with carbon electrode. *Nano Lett.* **2015**, *15*, 2402−2408.
(41) Islam, M. B.; Yanagida, M.; Shirai, Y.; Nabetani, Y.; Miyano, K. NiO_x hole transport layer for perovskite solar cells with improved stability and reproducibility. *ACS Omega* **2017**, *2*, 2291−2299.
(42) Hu, R.; Zhang, R.; Ma, Y.; Liu, W.; Chu, L.; Mao, W.; Zhang, J.; Yang, J.; Pu, Y.; Li, X. Enhanced hole transfer in hole-conductor-free perovskite solar cells via incorporating cus into carbon electrodes. *Appl. Surf. Sci.* **2018**, *462*, 840−846.
(43) Haque, M. A.; Sheikh, A. D.; Guan, X.; Wu, T. Metal oxides as efficient charge transporters in perovskite solar cells. *Adv. Energy Mater.* **2017**, *7*, No. 1602803.
(44) Nouri, E.; Mohammadi, M. R.; Lianos, P. Construction of perovskite solar cells using inorganic hole-extracting components. *ACS Omega* **2018**, *3*, 46−54.
(45) Islam, M. B.; Yanagida, M.; Shirai, Y.; Nabetani, Y.; Miyano, K. NiO_x Hole transport layer for perovskite solar cells with improved stability and reproducibility. *ACS Omega* **2017**, *2*, 2291−2299.
(46) Zhou, L.; Zuo, Y.; Mallick, T. K.; Sundaram, S. Enhanced efficiency of carbon-based mesoscopic perovskite solar cells through a tungsten oxide nanoparticle additive in the carbon electrode. *Sci. Rep.* **2019**, *9*, No. 8778.
(47) Granqvist, C. G. Oxide electrochromics: An introduction to devices and materials. *Sol. Energy Mater. Sol. Cells* **2012**, *99*, 1−13.
(48) Cannavale, A.; Eperon, G. E.; Cossari, P.; Abate, A.; Snaith, H. J.; Gigli, G. Perovskite photovoltachromic cells for building integration. *Energy Environ. Sci.* **2015**, *8*, 1578−1584.
(49) Roy, A.; Ghosh, A.; Bhnadari, S.; Selvaraj, P.; Sundaram, S.; Mallik, T. K. Color comfort evaluation of dye-sensitized solar cell (DSSC) based building-integrated photovoltaic (BIPV) glazing after 2 years of ambient exposure. *J. Phys. Chem. C* **2019**, *123*, 23834−23837.
(50) Mei, A.; Li, X.; Liu, L.; Ku, Z.; Liu, T.; Rong, Y.; Xu, M.; Hu, M.; Chen, J.; Yang, Y.; Grätzel, M.; Han, H. A hole-conductor−free, fully printable mesoscopic perovskite solar cell with high stability. *Science* **2014**, *345*, 295−298.
(51) Xiong, Y.; Zhu, X.; Mei, A.; Qin, F.; Liu, S.; Zhang, S.; Jiang, Y.; Zhou, Y.; Han, H. Bifunctional Al_2O_3 interlayer leads to enhanced open-circuit voltage for hole-conductor-free carbon-based perovskite solar cells. *Sol. RRL* **2018**, *2*, No. 1800002.
(52) Senthilarasu, S.; Fernández, E. F.; Almonacid, F.; Mallick, T. K. Effects of spectral coupling on perovskite solar cells under diverse climatic conditions. *Sol. Energy Mater. Sol. Cells* **2015**, *133*, 92−98.
(53) Stubhan, T.; Li, N.; Luechinger, N. A.; Halim, S. C.; Matt, G. J.; Brabec, C. J. High fill factor polymer solar cells incorporating a low temperature solution processed WO_3 hole extraction layer. *Adv. Energy Mater.* **2012**, *2*, 1433.
(54) Yi, H.; Wang, D.; Duan, L.; Haque, F.; Xu, C.; Zhang, Y.; Conibeer, G.; Uddin, A. Solution-processed WO_3 and water-free PEDOT:PSS composite for hole transport layer in conventional perovskite solar cell. *Electrochim. Acta* **2019**, *319*, 349−358.
(55) Vemuri, R. S.; Bharathi, K. K.; Gullapalli, S. K.; Ramana, C. V. Effect of Structure and size on the electrical properties of nanocrystalline WO_3 films. *ACS Appl. Mater. Interfaces* **2010**, *2*, 2623−2628.
(56) Gillet, M.; Lemire, C.; Gillet, E.; Aguir, K. The role of surface oxygen vacancies upon WO_3 conductivity. *Surf. Sci.* **2003**, *532*−*535*, 519−525.
(57) Granqvist, C. G. Electrochromic tungsten oxide films: review of progress 1993-1998. *Sol. Energy Mater. Sol. Cells* **2000**, *60*, 201−262.
(58) Ku, Z.; Rong, Y.; Xu, M.; Liu, T.; Han, H. Full printable processed mesoscopic $CH_3NH_3PbI_3/TiO_2$ heterojunction solar cells with carbon counter electrode. *Sci. Rep.* **2013**, *3*, No. 3132.
(59) Chan, C.-Y.; Wang, Y.; Wu, G.-W.; Wei-Guang Diau, E. Solvent-extraction crystal growth for highly efficient carbon-based mesoscopic perovskite solar cells free of hole conductors. *J. Mater. Chem. A* **2016**, *4*, 3872−3878.
(60) Liu, S.; Cao, K.; Li, H.; Song, J.; Han, J.; Shen, Y.; Wang, M. Full printable perovskite solar cells based on mesoscopic $TiO_2/Al_2O_3/NiO$ (carbon nanotubes) architecture. *Sol. Energy* **2017**, *144*, 158−165.

DOI: 10.1021/acsomega.9b02934
ACS Omega 2020, 5, 422−429